Noise analysis and improvement of displacement vector estimation from angular displacements

Hao Chen
Department of Medical Physics and Department of Electrical and Computer Engineering, University of Wisconsin—Madison, 1300 University Avenue, 1530 MSC, Madison, Wisconsin 53706

Tomy Varghese[a)]
Department of Medical Physics, University of Wisconsin—Madison, 1300 University Avenue, 1530 MSC, Madison, Wisconsin 53706

(Received 11 September 2007; revised 29 February 2008; accepted for publication 6 March 2008; published 25 April 2008)

Elastography or elasticity imaging techniques typically image local strains or Young's modulus variations along the insonification direction. Recently, techniques that utilize angular displacement estimates obtained from multiple angular insonification of tissue have been reported. Angular displacement estimates obtained along different angular insonification directions have been utilized for spatial-angular compounding to reduce noise artifacts in axial-strain elastograms, and for estimating the axial and lateral components of the displacement vector and the corresponding strain tensors. However, these angular strain estimation techniques were based on the assumption that noise artifacts in the displacement estimates were independent and identically distributed and that the displacement estimates could be modeled using a zero-mean normal probability density function. Independent and identically distributed random variables refer to a collection of variables that have the same probability distribution and are mutually independent. In this article, a modified least-squares approach is presented that does not make any assumption regarding the noise in the angular displacement estimates and incorporates displacement noise artifacts into the strain estimation process using a cross-correlation matrix of the displacement noise artifacts. Two methods for estimating noise artifacts from the displacement images are described. Improvements in the strain tensor (axial and lateral) estimation performance are illustrated utilizing both simulation data obtained using finite-element analysis and experimental data obtained from a tissue-mimicking phantom. Improvements in the strain estimation performance are quantified in terms of the elastographic signal-to-noise and contrast-to-noise ratios obtained with and without the incorporation of the displacement noise artifacts into the least-squares strain estimator. [DOI: 10.1118/1.2905024]

Key words: displacement, elastography, elastogram, elasticity, elasticity imaging, strain, ultrasound

I. INTRODUCTION

Elastography or elasticity imaging techniques that image the local stiffness properties of tissue are relatively new techniques for noninvasive investigation of tissue mechanical properties.[1–9] In conventional elastographic imaging, tissue is deformed using a quasistatic compression, with pre-and post-compression radio-frequency (rf) data frames acquired. Local strains are computed from the gradient of the displacement field along the axial direction between the pre- and postcompression echo signal frames. Local strain images are interpreted based on the fact that stiffer tissues deform less than softer tissues under identical compressional forces and similar boundary conditions, thereby providing a relative comparison of the stiffness variations in tissue.

Local tissue displacements along the beam direction could be estimated using classical time delay estimation techniques. Thus, strains along the insonification direction, which is typically along the ultrasound beam direction, are estimated. Spatial-angular compounding for elastography was also recently introduced to reduce noise artifacts in elastograms, by averaging multiple strain estimates around the same region of interest (ROI) acquired from different insonification angles.[10,11] The noise artifacts present in the displacement estimate include jitter and peak-hopping artifacts. Signal decorrelation artifacts due to nonuniform and/or large applied compressions leading to out-of-plane motion may also be present. In addition, reduction in the ultrasound signal-to-noise ratio due to attenuation and geometric distortion due to beam steering may also be present. Our approach reduces noise artifacts due to the signal processing algorithm, peak hopping, decorrelation, and increased nonstationary noise due to the applied compression. Our results demonstrate the improvement in the elastographic signal-to-noise ratio (SNR_e) and elastographic contrast-to-noise ratio (CNR_e) obtained with angular compounding. We have also demonstrated angular compounding methods that do not require the incompressibility assumption.[12]

In addition, axial and lateral components of the displacement vector can also be estimated from the angular displacements obtained. Estimation of lateral and shear strains provides useful information for clinical diagnosis regarding lesion mobility assessments.[10–15] Techavipoo *et al.*[10,11] previ-

ously described a least-squares method to reduce noise in the axial strain image and for the estimation of lateral strains at different angular insonifications using a phased array transducer. A similar analysis using a linear array transducer with electronic beam steering was also presented by Rao and Varghese.[12,14]

However, both angular compounding and lateral strain estimation techniques introduced above assume that the noise in the angular displacement estimates can be modeled using a zero-mean normal probability density function and that the displacement noise artifacts are independent and identically distributed (i.i.d.). In this article, we describe a modified and improved least-squares method for the estimation of the axial and lateral strains from the angular displacement data that does not make any assumptions regarding displacement noise artifacts. This is done by utilizing a cross-correlation matrix that incorporates the impact of the displacement noise artifacts into the modified least-squares algorithm. We also present two methods that can be utilized for estimating the displacement noise artifacts from estimated displacement images.

In this article, we present improved displacement (axial and lateral) vector and strain (axial and lateral) tensor estimation performance utilizing both ultrasound simulations and experimental data obtained from tissue-mimicking (TM) phantoms, using the modified least-squares method. Improvements in the strain estimation performance are quantified in terms of the SNR_e and CNR_e obtained with and without the incorporation of the displacement noise artifacts into the least-squares strain estimator.

II. THEORY

II.A. Least-squares method for angular compounding

The quasistatic compression or mechanical stimulus for elastography is applied along the z-axis, also referred to as the axial direction. The lateral direction or x-axis is defined as the direction orthogonal to the axial direction and located within the imaging plane. Consider the motion tracking of an actual displacement vector $\vec{d}$ at point O in space observed using a 1D linear array transducer with beam steering as shown in Fig. 1. Let $\vec{u}_\theta$ denote the unit vector along the A-line or insonification direction for the B-mode or rf data frame with a beam angle θ that passes though point O. The dot product p_θ between $\vec{d}$ and $\vec{u}_\theta$ can be written as

$$p_\theta = \vec{d} \cdot \vec{u}_\theta = d_z \cos\theta + d_x \sin\theta, \tag{1}$$

where d_z and d_x are components of the displacement vector $\vec{d}$ in the z and x directions, while $\cos\theta$ and $\sin\theta$ are the components of the unit vector $\vec{u}_\theta$ in the z and x directions, respectively. Let q_θ be an observation of the displacement vector $\vec{d}$ obtained using the pre- and postcompression rf data obtained along the θ beam insonification direction for the motion vector $\vec{u}_\theta$. This observed displacement can be written as

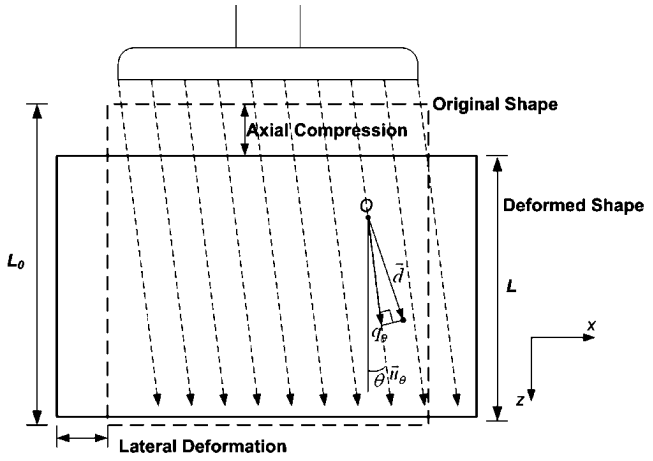

FIG. 1. Schematic diagram illustrating the tracking of the actual displacement (vector $\vec{d}$) at a point O in the angular displacement field.

$$q_\theta = d_z \cos\theta + d_x \sin\theta + n_\theta, \tag{2}$$

where n_θ denotes the noise in the observations of the angular displacement estimate. In ultrasound elastography, q_θ denotes the displacement estimate obtained using cross correlation between the overlapped and gated windows of the pre- and postcompression rf echo signals along the θ insonification direction. Techavipoo *et al.*[11] have modeled the errors in the displacement estimates as randomly distributed additive Gaussian white noise.

Local tissue displacements are estimated using multiple angular beams at different insonification angles passing through point O, with each insonification angle providing a single observation of the displacement. Thus, for multiple insonification angles, let $\vec{u}_{\theta_i}$ denote the motion vector along the A-line at beam angle θ_i passing through point O for $i = 1, 2, \ldots, m$, where m is the total number of insonification angles. In a similar manner n_{θ_i} is the noise in the observation at angle θ_i. Rewriting these equations in a matrix form, we obtain

$$\vec{q} = A\vec{d} + \vec{n}, \tag{3}$$

where

$$\vec{q} = \begin{bmatrix} q_{\theta_1} \\ q_{\theta_2} \\ \vdots \\ q_{\theta_m} \end{bmatrix},$$

$$A = \begin{bmatrix} \cos(\theta_1) & \sin(\theta_1) \\ \cos(\theta_2) & \sin(\theta_2) \\ \vdots & \vdots \\ \cos(\theta_m) & \sin(\theta_m) \end{bmatrix},$$

$$\vec{d} = \begin{bmatrix} d_z \\ d_x \end{bmatrix},$$

$$\vec{n} = \begin{bmatrix} n_{\theta_1} \\ n_{\theta_2} \\ \vdots \\ n_{\theta_m} \end{bmatrix}, \tag{4}$$

where $\vec{d}$ denotes the axial and lateral displacement components of the displacement vector associated with the observed angular displacement $\vec{q}$ to be estimated. Now, let $\tilde{d}$ denote the displacement vector estimated from the angular observation data $\vec{q}$. The squared error between the estimated displacement $\tilde{d}$ and the measurement $\vec{q}$ can be expressed as

$$\begin{aligned} e &= \|\vec{q} - A\tilde{d}\|^2 = (\vec{q} - A\tilde{d})^T(\vec{q} - A\tilde{d}) \\ &= \vec{q}^T\vec{q} - \vec{q}^TA\tilde{d} - \tilde{d}^TA^T\vec{q} + \tilde{d}^TA^TA\tilde{d}. \end{aligned} \tag{5}$$

To minimize the squared error in Eq. (5), the first derivative of e with respect to the estimated displacement $\tilde{d}$ should be equal to zero,

$$\frac{\partial e}{\partial \tilde{d}} = -2A^T\vec{q} + 2A^TA\tilde{d} = 0. \tag{6}$$

Finally, the least-squares solution (LS) obtained by Techavipoo *et al.*[11] is given by

$$\tilde{d} = (A^TA)^{-1}A^T\vec{q} = (A^TA)^{-1}A^T(A\vec{d} + \vec{n}) = \vec{d} + K\vec{n}, \tag{7}$$

where

$$K = (A^TA)^{-1}A^T = \begin{bmatrix} \vec{k}_z \\ \vec{k}_x \end{bmatrix},$$

$$\vec{k}_z = \begin{bmatrix} k_{z_1} & k_{z_2} \cdots k_{z_m} \end{bmatrix}, \quad \vec{k}_x = \begin{bmatrix} k_{x_1} & k_{x_2} \cdots k_{x_m} \end{bmatrix},$$

where σ_{θ_i} is the standard deviation of the noise n_{θ_i} in the angular displacement estimates. The displacement estimate along the z or axial direction can be written as

$$\tilde{d}_z = d_z + n_z, \tag{8}$$

$$n_z = \sum_{i=1}^{m} k_{z_i} n_{\theta_i}, \tag{9}$$

$$\sigma_z = \sqrt{\sum_{i=1}^{m} k_{z_i}^2 \sigma_{\theta_i}^2}, \tag{10}$$

where σ_z is the standard deviation of the displacement noise after the least-squares minimization to obtain the component of the displacement vector along the z direction. The displacement noise n_z is a linear combination of the noise n_{θ_i} in each angular displacement estimates as shown in Eq. (9). Therefore, σ_z is given by a function of k_{z_i} and σ_{θ_i} as shown in Eq. (10). In a similar manner, the displacement estimate along the x or lateral direction is given by

$$\tilde{d}_x = d_x + n_x, \tag{11}$$

$$n_x = \sum_{i=1}^{m} k_{x_i} n_{\theta_i}, \tag{12}$$

$$\sigma_x = \sqrt{\sum_{i=1}^{m} k_{x_i}^2 \sigma_{\theta_i}^2}, \tag{13}$$

where σ_x is the standard deviation of the displacement noise after the least-squares minimization to obtain the component of the displacement vector along the x or lateral direction. In a similar manner, σ_x is given by the function of k_{x_i} and σ_{θ_i} shown as Eq. (13).

We utilize linear interpolation for image registration of the angular displacement data to a Cartesian spatial grid constructed for the zero-angle displacement data. Since angular displacement images at different insonification angles have different pixel grid locations, bilinear interpolation is utilized to register the angular displacement estimates. Under the assumption that the angular displacement images are locally smooth, linear interpolation can be used to interpolate angular observations onto pixels of the zero-angle grid.

The LS method to estimate the displacement vectors from the angular displacement data is an optimal solution for the value of $\vec{d}$ only when the noise in the angular displacement estimates follow a Gaussian distribution and are i.i.d. random variables in the observation at each angle θ_i. However, the noise artifacts in the tissue displacement estimates obtained using cross-correlation analysis between the overlapped windows of pre- and postcompression rf echo signals, although they follow a Gaussian distribution,[11] are not i.i.d. The noise artifacts are not i.i.d. since they increase with insonification angle,[11] as depicted in the angular elastograms. This increase in noise is due to the compression direction being along the 0° insonification angle, while displacement estimations are performed along the θ insonification direction (the noise increases with an increase in θ).[11] In addition, the largest component of the axial displacement would lie along the 0° insonification direction. For all other insonification angles the angular displacement contains components of both axial and lateral displacements, with the axial component reducing with an increase in the angle and the lateral displacement being maximized at a 90° insonification angle, respectively. This aspect is clearly illustrated in Fig. 1, which presents the direction of compression and the components of the displacement vector. An illustration of the increased noise artifacts in the displacements obtained along each beam-steered angle θ_i and their variability at each angle are illustrated in Sec. III.

II.B. Modified and improved least-squares method for non-i.i.d. noise

Derivation of the modified least-squares algorithm when the noise artifacts are no longer i.i.d. is described below. We illustrate that, if the cross-correlation matrix of the noise at each angle θ_i can be calculated, the optimal solution for the value of the displacement vectors $\vec{d}$ can be obtained using the LS algorithm.

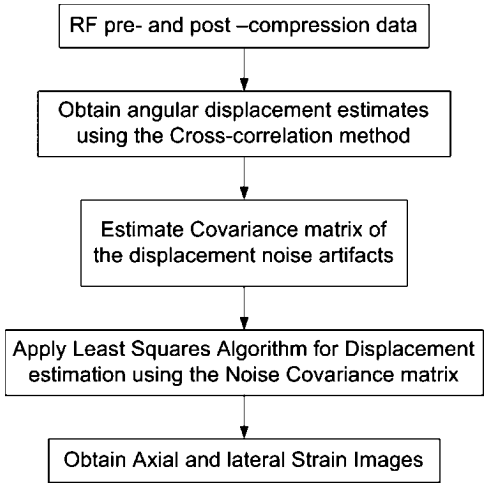

FIG. 2. Flowchart of the least-squares method that incorporates the cross-correlation noise matrix.

Let C_n denote the cross-correlation matrix with the non-i.i.d. noise artifacts $\vec{n}$ along different angular insonification directions. The matrix C_n is a full-rank symmetric matrix. The non-i.i.d. noise $\vec{n}$ can be expressed as a product of independent identically distributed Gaussian noise with zero mean and unit variance and a matrix B that accounts for the non-i.i.d. nature of the noise artifacts (see Appendix A for details) as shown below:

$$\vec{n} = B\vec{n}_{\mathrm{gd}}, \tag{14}$$

where $\vec{n}_{\mathrm{gd}}$ denotes the zero-mean i.i.d. and Gaussian distributed noise, and the matrix B is obtained from the relationship $C_n = BB^T$. The details regarding the construction of matrix B from the noise cross-correlation matrix C_n are described in Appendix A. Equation (3) relating the angular displacement observations to the actual orthogonal components of the displacement vector can now be rewritten as

$$\vec{q} = A\vec{d} + \vec{n}_{\mathrm{gd}}, \tag{15}$$

$$B^{-1}\vec{q} = B^{-1}A\vec{d} + B^{-1}B\vec{n}_{\mathrm{gd}} = B^{-1}A\vec{d} + \vec{n}_{\mathrm{gd}} = D\vec{d} + \vec{n}_{\mathrm{gd}}. \tag{16}$$

In a similar manner as illustrated in Eqs. (3)–(7), the estimated displacement vectors are given by

$$\begin{aligned}\tilde{\vec{d}} &= (D^TD)^{-1}D^T(B^{-1}\vec{q}) \\ &= ((B^{-1}A)^T(B^{-1}A))^{-1}((B^{-1}A))^TB^{-1}(A\vec{d} + \vec{n}) \\ &= \vec{d} + K\vec{n},\end{aligned} \tag{17}$$

where $D = B^{-1}A$ and $K = (D^TD)^{-1}D^TB^{-1}$.

Equation (17) provides orthogonal displacement vector estimates with non-i.i.d. noise artifacts when compared to Eq. (7), where the noise artifacts in the displacement estimates have to be i.i.d. and follow a Gaussian distribution. The solution provided in Eq. (17) represents a general purpose solution for the estimation of orthogonal displacement vectors from the angular displacement observations. Figure 2 presents a flow chart of the improved general purpose least-squares method that improves the accuracy of displacement estimation by utilizing an estimated noise covariance matrix. The following subsection present methods that can be utilized to estimate the noise properties and thereby the cross-correlation or covariance noise matrix of the local displacement field.

II.C. Noise estimation from the displacement field

Noise artifacts in the tissue displacement field can be calculated if the exact noise-free displacement fields are available (for example with finite-element analysis). However, the actual noise-free displacement fields are generally not available in practice. Noise artifacts in the displacement field, however, can be estimated for uniformly elastic media from the standard deviation or variance of the displacement estimates for a known applied compression under specified boundary conditions. However, for inhomogeneous media, estimation of the noise artifacts is significantly more difficult. Methods to estimate the noise artifacts are therefore essential for the computation of the noise covariance matrix. In this article, we present two different methods that can be utilized to estimate the noise artifacts from tissue displacement estimates. The performance of both these methods will be evaluated experimentally using a uniformly elastic tissue-mimicking phantom.

A uniformly elastic phantom with a known applied compression and under slip boundary conditions is utilized to generate displacement and strain images. The actual displacement p_θ for a specific insonification angle θ of the uniformly elastic phantom is continuous for a uniform applied compression, even through the value of the displacement vector p_θ depends on its location within the phantom. Increased lateral displacements occur in regions away from the axis of compression (typically along the phantom center), which are observed toward the edges of the displacement and strain images as increased signal decorrelation artifacts.[16] The derivative of the displacement with respect to z and x (axial and lateral) coordinates is also continuous since the local strain in a uniform phantom is continuous under a constant applied compression. Therefore, all the angular observations q_θ can be regarded as data points on a smooth angular displacement curve that is corrupted with the additive Gaussian noise. The first method proposed for noise estimation uses a second-order polynomial fit to reconstruct the smooth curve in the presence of the angular displacement observations. The noise artifacts can be estimated from the difference between the reconstructed smooth curve and actual estimated angular displacement values.

The second method utilizes a two-dimensional adaptive Wiener filter to estimate noise artifacts in the displacement field. This method reduces the entire displacement image into a number of smaller blocks and estimates noise in the selected blocks with identical value.[17] Adaptive Wiener filtering methods described by Ozkan *et al.*[18] and Olsen[17] are potentially efficient methods for estimating noise in the displacement image. The Wiener filter is a mean-square error (MSE), i.e., an optimal stationary linear filter for images de-

graded by additive noise and blurring artifacts. However, the application of the Wiener filter requires the assumption that the image and noise are second-order stationary. The Wiener filter works very well when the noise is constant power (i.e., white), such as Gaussian noise.[19] Adaptive Wiener filtering, however, is more selective than the polynomial curve-fitting method, preserving details and other additional high-frequency content within the image, which are present in inhomogeneous tissue. In this article, both of these methods are evaluated to estimate noise in the displacement image.

III. SIMULATION RESULTS

III.A. Method

In this section we evaluate the performance of both the noise estimation methods using a simulated numerical phantom constructed using a commercial finite-element analysis (FEA) package ANSYS (ANSYS Inc., Pittsburgh, PA) and an ultrasound simulation program developed in our laboratory.[20] A uniformly elastic phantom with dimensions of $60\times60\times10$ mm^3 was meshed using the FEA program. The phantom was compressed using a uniform external deformation of 0.5% of the phantom height, after precompression increments of 1%, 1.5%, and 2%, respectively (the exact precompression increment utilized is described in the figure captions and the description of each figure) under slip boundary conditions using the FEA program and the corresponding displacement field obtained.

Pre- and postcompression ultrasound radio-frequency echo signals were then obtained using the frequency-domain ultrasound simulation program.[20] A linear array transducer was modeled that consisted of 0.1×10 mm elements with a 0.1 mm center-to-center separation. Each acoustic beam was formed using 64 consecutive elements. The incident pulses were modeled to be Gaussian shaped with a 5 MHz center frequency and an 80% bandwidth (full width at half-maximum). The speed of sound in the simulation was 1540 m/s, and the attenuation coefficient was set to 0.5 dB/cm/MHz. Tissue scatterers were modeled using 100 μm radius polystyrene beads, which were randomly distributed in the numerical phantom at a sufficient number density to obtain Rayleigh statistics. The postcompression rf data were obtained by incorporating the displacement field obtained using FEA analysis to displace the scatterer positions in response to the modeled mechanical stimuli described above. The simulated pre- and postcompression echo signals with different beam-steering angle were obtained and utilized to estimate noise artifacts in the displacement image.

Local displacements between the pre- and postcompression rf data are estimated using a 1D normalized cross-correlation method. Displacement estimates are obtained from the shift in the peak of the normalized cross-correlation function. A rectangular gated window length of 3 mm with a 75% overlap between the data segments was utilized to obtain local displacement estimates.

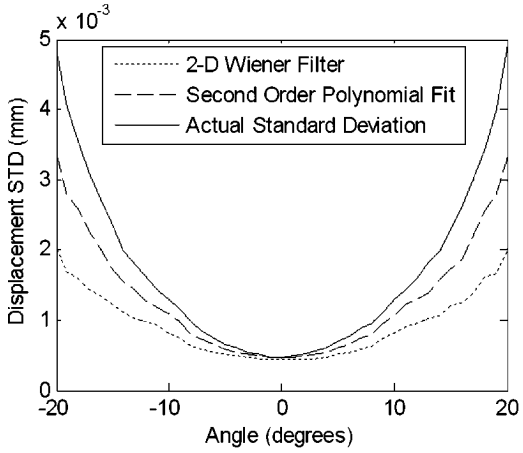

FIG. 3. Standard deviation of the displacement estimates for the simulated uniformly elastic phantom. Both the adaptive 2D Wiener filtering and second-order polynomial fit methods are utilized to estimate the noise artifacts. The actual displacement errors at different insonification angles θ_i are also presented as a comparison to the displacement noise estimated using the two methods described above. The applied compression was 0.5% of the phantom height along with a 2% precompression increment.

III.B. Results

A comparison of the standard deviation in the displacement estimates obtained using an adaptive Wiener filter and a second-order polynomial fit along with the actual standard deviation of the displacement field in the uniformly elastic phantom is illustrated in Fig. 3. The noise estimation for all the methods described above is performed in a 50×50 mm^2 region located at the center of the phantom. The applied compression in the phantom was 0.5% of its height along with a 2% precompression increment. Since a uniformly elastic phantom was modeled with a specified applied compression, the standard deviation of the displacement estimates can be directly computed, and is plotted as the "actual standard deviation" as illustrated in Fig. 3. The displacement field of the uniformly elastic phantom increases linearly with depth to provide a fairly constant strain due to the applied compression. Since we utilize a linearly elastic phantom, and the applied compression is uniform, we can fit and remove the linear trend from the displacement estimates to obtain the actual standard deviation of the displacement estimates.

Both the adaptive Wiener filter and the second-order polynomial fit provide estimates of the displacement noise or standard deviation with a smaller value when compared to the standard deviation of actual errors in the estimated displacement. The adaptive Wiener filter underestimates the standard deviation of the displacement noise when compared to the second-order polynomial fit. However, the standard deviation of the displacement errors obtained with all the methods increases with an increase in the beam-steering angle as illustrated in Fig. 3. The standard deviation curve relative to the beam-steering angle shows a similar trend for all the methods. Therefore, both of these methods can be used to estimate the noise level of the displacement estimates relative to the beam steering angle. These methods are useful

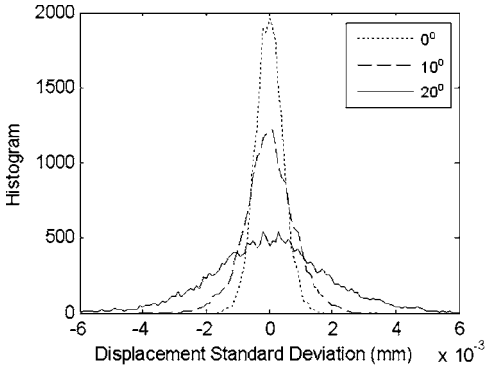

FIG. 4. Histogram of the estimated displacement noise artifacts at different insonification angles θ_i obtained using the simulated uniformly elastic phantom.

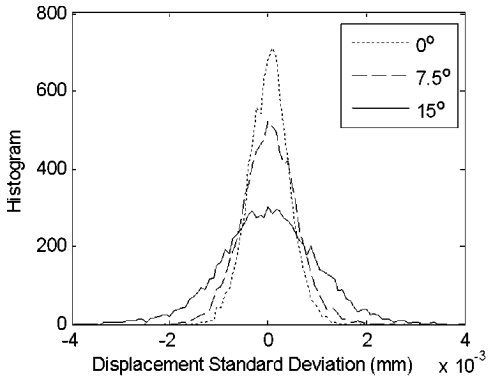

FIG. 5. Histogram of estimated displacement noise artifacts at different insonification angles θ_i obtained using a uniformly elastic TM phantom. The displacement noise was estimated using the 2D adaptive Wiener filtering method.

since they can be utilized to estimate displacement noise artifacts in inhomogeneous phantoms or biological tissue where the actual standard deviation of the displacement estimates are more difficult to estimate.

Figure 4 presents a histogram of the displacement errors (standard deviation) obtained using a 2D 7×7 pixel adaptive Wiener filter for different beam-steering angles. Observe that the distributions of the displacement noise obtained at different insonification angles θ_i are not identical, with the spread in the noise artifacts increasing with beam-steering angle. The noise at each insonification angle θ_i can be fit to a Gaussian distribution with a zero mean. However, the variance or standard deviation of the Gaussian distribution increases with an increase in the beam steering or insonification angle. This result illustrates the non-i.i.d. nature of the displacement noise artifacts for the estimation of angular strain estimates, which are also corroborated by the experimental results in the next section.

IV. EXPERIMENTAL RESULTS

IV.A. Method

A uniformly elastic tissue-mimicking (TM) phantom with dimensions of $90\times90\times90$ mm^3 was used for experimental validation.[21] The Young's modulus of the TM material was 30 KPa measured using the ELF 3200 mechanical testing system (EnduraTEC, Minnetonka, MN) in our laboratory. The TM material for the phantom consists of gelatin with a suspension of microscopic safflower oil droplets. The Young's modulus of the TM material reduces with an increase in the concentration of the safflower oil droplets, and thimerosal is utilized as the preservative.[21]

The TM phantom was immersed in a safflower oil bath and scanned using a real-time clinical Siemens Antares Ultrasound Scanner (Siemens Medical Solutions USA, Inc., Ultrasound Division, Issaquah, WA), using a linear array transducer (VFX 9–4) with a center frequency of 8.99 MHz and 70% bandwidth. A single transmit focus was set at a depth of 4 cm in the phantom with dynamic focusing on receive. The linear array transducer provided 360 *A*-lines within a single rf data frame at a 40 MHz sampling rate. The rf data were acquired using the Axius direct ultrasound research interface (URI) on the scanner and transferred to a personal computer for off-line analysis

A compression plate with a rectangular slot that matches the transducer face was mounted on a linear translation stage driven by a computer-controlled stepper motor. The compression plate was larger than the phantom surface, and provides a uniform compression of the phantom. Echo signals were acquired originating from the top of the phantom to a depth of 5 cm before and after an axial applied compression of 0.5%, 1%, 1.5%, and 2% of the phantom height, respectively. An initial precompression of 3 mm (3.33%) was applied to ensure proper contact between the compression plate and the phantom. The placement of the phantom in the safflower oil bath also provides a thin film of oil on the top and bottom surfaces of the phantom to ensure slip boundary conditions. Angular radio-frequency data frames are acquired before and after compression using beam steering over insonification angles of $\pm20°$ in 1° increments. The entire experiment was repeated ten times at different locations on the phantom to obtain independent rf data realizations to obtain statistically significant results.

IV.B. Results

Angular rf pre- and postcompression data frames were analyzed using the 1D normalized cross-correlation method using a 12-wavelength (2.1 mm) rectangular gated window with a 75% overlap between subsequent windows. Figure 5 presents a histogram of the displacement errors in the angular displacement estimates using a 2D 7×7 pixel adaptive Wiener filter. Note that the distributions of noise at the different insonification angles θ_i are not identical, even though the noise at each insonification angle θ_i can be fitted to a Gaussian distribution with a zero mean. The variance of Gaussian distribution increases with an increase in the insonification angle in a similar manner as illustrated in the simulation results in Fig. 4. Similar results as those shown in Fig. 5, are obtained when the second-order polynomial fit is utilized to estimate displacement noise artifacts.

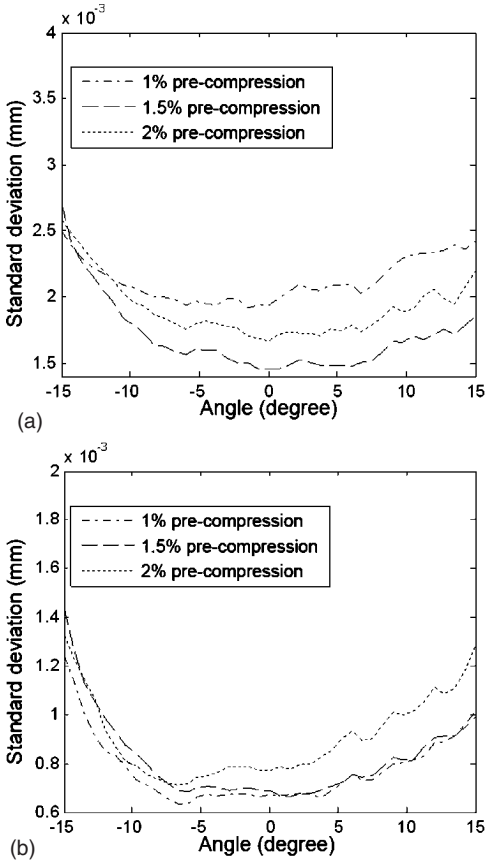

FIG. 6. Standard deviation of the estimated displacement noise artifacts at different insonification angles denoted by θ_i. The standard deviation of the displacement noise is plotted for an applied compression of 0.5% and for different precompression values of 1%, 1.5%, and 2%, respectively. The displacement noise shown in (a) is estimated using a second-order polynomial curve fit, while that in (b) is estimated using a 7×7 2D adaptive Wiener filter.

The standard deviation or displacement noise in the angular displacement images obtained at different insonification angles calculated using the two noise estimation techniques are illustrated in Fig. 6. Results obtained using the second-order polynomial curve fit are shown in Fig. 6(a), while Fig. 6(b) presents results obtained using the 7×7 pixel 2D adaptive Wiener filtering method, respectively. The data sets include three cases with different precompression levels as shown in Fig. 6. Note that the standard deviation of the estimated displacement noise using the second-order polynomial fit is almost two times that obtained using adaptive Wiener filtering for the same angular displacement data set.

This result is consistent in that adaptive Wiener filtering preserves small details and other high-frequency content in the displacement image. Note also that the standard deviation curves relative to the insonification angle θ_i from the same rf data with the different noise estimation methods have similar shapes. The standard deviation increases linearly with increases in the insonification angle θ_i in most cases. Since the noise in the displacement estimate increases with angle, it does not satisfy the i.i.d. property for the LS algorithm. These simulation and experimental results demonstrate that the two noise estimation algorithms can be utilized to estimate displacement noise artifacts especially in inhomogeneous media enabling the utilization of the modified LS algorithm described in this article. The modified LS algorithm, described in the next section, utilizes the estimate of the noise artifacts to derive a cross-correlation or covariance noise matrix to improve the accuracy of displacement estimation.

IV.C. The modified least-squares method for strain estimation

Ultrasound pre- and postcompression angular radio-frequency data on TM phantoms are obtained in a manner similar to that described in the previous section. A uniformly elastic phantom is utilized to obtain data to compute the mean and variance of the resulting strain image and to calculate the corresponding elastographic SNR_e obtained. A single inclusion TM phantom with dimensions of $90\times90\times90$ mm^3 with a 10 mm diameter cylindrical inclusion at a 35 mm depth is also utilized to obtain a quantitative comparison of the CNR_e for the two LS methods.[21] The inclusion is 3 times stiffer than the background. Each experiment was repeated ten times with data acquisition performed at different location in the phantom as described previously. Finally, the mean and the standard deviations of the SNR_e, and CNR_e parameters obtained are compared for the two LS methods.

Figures 7(a) and 7(b) present plots of the SNR_e along the axial and lateral direction versus the applied compression for both the LS methods. Error bars in the plots shown in Figs. 7–9 with the short, medium, and long bars on the top correspond to the standard LS, LS plus second-order polynomial, and LS plus 2D Wiener filter, respectively. Note the significant improvement in the SNR_e obtained using the improved LS method, where the covariance noise matrix estimated using both the second-order polynomial fit and the 2D Wiener filter have been utilized as shown in the figure. Observe that for both the LS methods the SNR_e reduces with applied compression; however, for the LS method without noise estimation the drop-off in the SNR_e is significant. Both the methods utilized for estimation of the displacement noise appear to provide similar results for the variation in the SNR_e with applied compression. Figures 7(c) and 7(d) presents the mean and the standard deviation of the improvement in the SNR_e along axial and lateral direction versus the applied compression for both the LS methods. The modified LS method shows significant improvement of the elastographic SNR_e along both axial and lateral directions. The improvement is more significant when the applied compression is larger than 1%.

In a similar manner, the variations in the CNR_e obtained using the inclusion phantom is presented in Figs. 8 and 9. As mentioned in the previous section, a second-order polynomial fit does not efficiently estimate noise in nonuniform displacement data, so only the 2D Wiener filter was applied to the data with the cylindrical inclusion to estimate noise. The ROIs in the strain image corresponding to the inclusion and the background that are utilized in the computation of the CNR_e are shown in Fig. 8. The strain images shown in

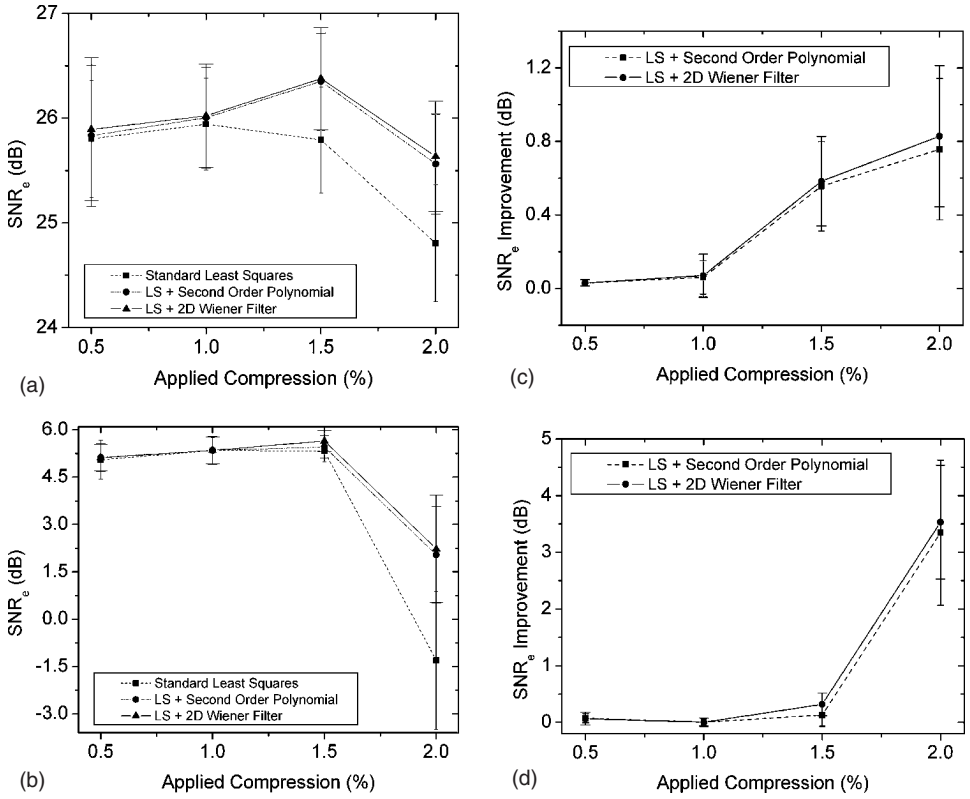

FIG. 7. Plots of elastographic SNR_e vs the applied compression for both the LS methods. Note that the improved LS method that utilizes the noise estimation performs significantly better than the standard LS method. The SNR_e variation is plotted for the (a) axial strain and (b) lateral strain estimates. The mean and standard deviation of the improvement were obtained over ten independent experiments for the (c) axial strain and (d) lateral strain estimates.

Fig. 8 are obtained using an applied compression of 2% of the phantom height. Both the LS methods use 41 sets of radio-frequency data frames acquired before and after compression using beam steering with insonification angles over a $\pm 20°$ range with 1° angular increments. Figure 8 presents the axial and lateral strain image using the modified LS method with covariance noise estimation [Fig. 8(a)] and the original method [Fig. 8(b). Noise estimation was performed using the 2D Wiener adaptive method since the phantom with an inclusion was utilized in Fig. 8. However, for the 20° maximum angle utilized in our experiment, Eqs. (1) and (2) indicate that only limited information on the lateral displacement d_x is present in q_θ, the angular displacements estimated. Therefore, the lateral strain images obtained contain additional noise artifacts. The trapezoidal region shown in Fig. 8 represents the region over which all the angular displacement estimates are available and utilized to compute the axial and lateral displacement vectors and subsequently the strain tensors.

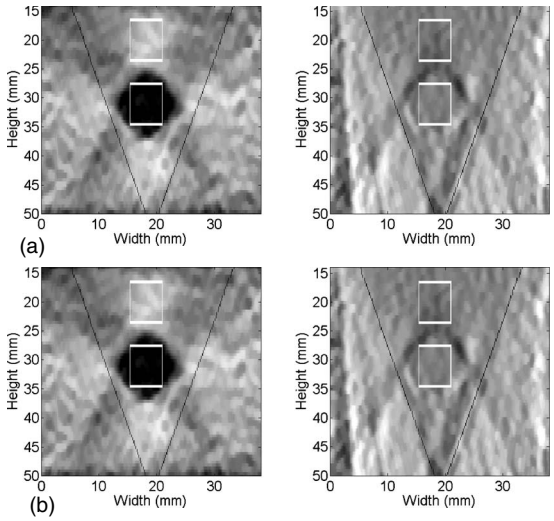

FIG. 8. Diagram illustrating the ROI utilized in the axial strain image and lateral strain image utilized to compute the CNR_e estimate for the modified LS method (a) and the original LS method (b). The axial and lateral strain images for the modified least-squares method were generated with noise estimated using adaptive 2D Wiener filtering of the displacement estimates.

Figure 9(a) presents plots of the CNR_e versus the applied compression for the LS method with and without the Wiener adaptive noise estimation. Note that the LS method with the noise estimation improves the CNR_e by about 0.35–0.89 dB at the different applied compressions. Observe the reduction in the CNR_e for the strain image obtained using the regular LS method without noise estimation with an increase in the applied compression, while the CNR_e estimates for the strain image obtained using the LS method with noise estimation remains fairly constant over all the applied compressions. Figure 9(b) presents the mean and the standard deviation of the improvement in the CNR_e versus the applied compression for both the LS methods. The mean and standard deviation is calculated using ten independent data sets.

V. DISCUSSION

In this article we demonstrate the impact of the non-i.i.d. nature of the angular displacement noise artifacts for axial and lateral strain estimation. In the earlier analysis,

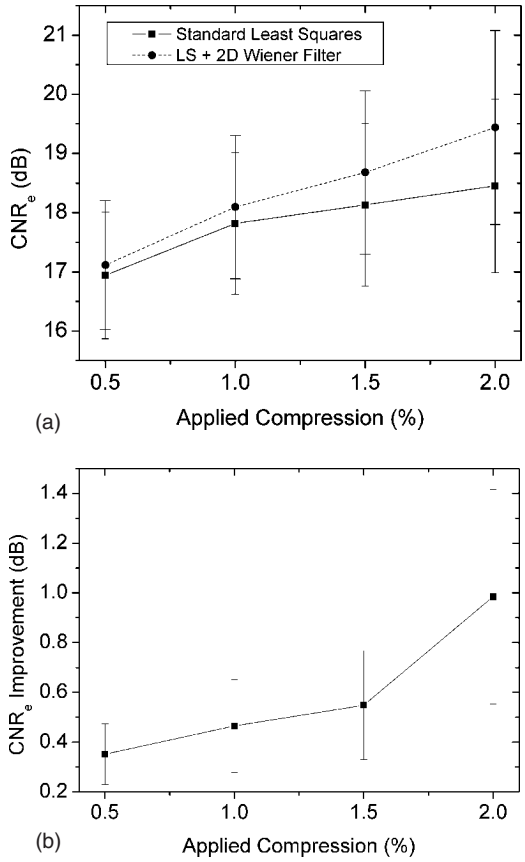

FIG. 9. Plots of (a) CNR_e variations vs the applied compression for both the standard and improved LS method incorporating noise estimation. The adaptive 2D Wiener filtering method was utilized for displacement noise estimation. The mean and standard deviation of the improvement in the CNR_e obtained using the modified LS method is shown in (b).

Techavipoo *et al.*[10,11] had presented a least-squares method to reduce noise in the axial strain image and the estimation of lateral strains at different angular insonifications using a phased array transducer. Estimation of the axial and lateral strains from the angular displacement data was done using a least-squares method that assumes a zero-mean Gaussian or normal distributed probability density function with the noise in the displacement estimates being i.i.d.

We show using both simulation and experimental results that the probability density function of the displacement noise at each insonification angle can be described by a Gaussian density function with zero mean. However, the variances of the displacement noise artifacts increase with the ultrasound beam-steering angle, making the assumption of i.i.d. noise in the previous analysis incorrect.

In this article, we introduce a modified least-squares technique that estimates the axial and lateral strain estimates after compensating for the non-i.i.d. nature of the displacement noise artifacts by incorporating a cross-correlation or covariance noise matrix. Displacement noise artifacts are estimated initially from the displacement estimates, using a second-order polynomial fit and a 2D adaptive Wiener filter. The cross-correlation matrix of the noise estimates are then incorporated into the modified least-squares algorithm to improve the strain estimation performance. Most of the computational time with this algorithm is for the estimation of the angular displacement, which takes 57 s for each pre- and postcompression data set. Computation of all the angular displacement data over the entire 41 angular insonification data sets therefore takes 39 min and 15 s. Additional computational aspects include interpolation of the displacement, estimation of the noise content, displacement compounding, and least-square strain estimation for a total of 47 min and 20 s for the entire procedure. The modified least-squares algorithm takes less than a second to estimate the noise level and calculate the matrix K, shown in Eq. (17), from the previously computed 41 angular displacement frames. Comparison of the two LS algorithms was performed on a PC with a 2.8 GHz Pentium 4 CPU and 1 GB of RAM with the code developed using MATLAB 7.1 software (The MathWorks, Natick, MA). We are, however, currently engaged in optimizing this process by acquiring data over fewer angular insonification directions by computing an optimal value of the insonification angle, which could lead to similar values of SNR_e in the elastograms using 5–10 angular data sets.

In this article a 1D normalized cross-correlation algorithm is utilized to estimate the angular displacements. The proposed method estimates the noise level of the local angular displacement and improves displacement vector estimation using the modified LS algorithm. Two-dimensional displacement estimation algorithms can also be utilized to estimate angular displacement and can provide a better spatial resolution along each insonification angle. However, displacement noise artifacts present in the images would still not be i.i.d., and the method proposed in this article can be applied in a similar manner to improve displacement vector and strain tensor estimation.

Simulation and experimental results demonstrate that the modified least-squares algorithm with noise characterization can significantly improve the SNR_e and CNR_e in both axial and lateral strain tensor images, since the noise estimation algorithm is applied to the displacement images that contain fewer pixels when compared to the rf data, which also significantly reduces the computational requirements of the modified least-squares algorithm for strain estimation.

VI. CONCLUSION

In this article we demonstrate the impact of the non-i.i.d. nature of the angular displacement noise artifacts relative to different beam insonification angles. We propose the use of a modified least-squares algorithm for angular strain estimation that utilizes a cross-correlation or covariance noise matrix that incorporates noise artifacts to further improve estimation of displacement vector and thereby the strain tensor components from the angular displacements. The method proposed in this article can be applied to the general inhomogeneous elastographic imaging situation, by utilizing algorithms such as the 2D adaptive Wiener filter to estimate displacement noise artifacts. The modified least-squares algorithm with noise characterization proposed in this article can be utilized to improve both spatial angular compounding

and lateral and shear strain estimation using the angular displacement data. Lateral and shear strain estimation is gaining importance, especially in the possible differentiation between benign and malignant masses based on their bonding properties to surrounding healthy tissue.[10–15] In addition, the reliability of Young's modulus reconstruction also improves with the utilization of all strain tensor (axial, lateral, and elevational) components.[22]

The modified LS algorithm described in this article is a general purpose algorithm that can be utilized with inhomogeneous strain distributions, as is generally the case with *in vivo* and experimental data. The modified LS method described in this article does not make any *a priori* assumptions regarding the noise content in the angular displacement estimates, and is particularly applicable for clinical imaging situations, where the displacement noise can be incorporated into the strain estimation process using a cross-correlation or covariance matrix. The proposed method for noise estimation can also be utilized in conjunction with other displacement estimation algorithms such as 2D or 3D cross-correlation or block-matching algorithms. In addition, the 2D adaptive Wiener filter utilized for noise estimation can be utilized for the general elastography problem. The 2D adaptive Wiener filter can be utilized to estimate the noise in the local displacements values, thereby evaluating the reliability[23] of the strain estimates obtained from the pre- and postcompression data sets.

ACKNOWLEDGMENTS

This work is supported by Komen Foundation Grant BCTR0601153 and NIH Grant R21 EB003853.

APPENDIX A: NOISE COVARIANCE MATRIX

Consider the noise $\bar{n}$ with the cross-correlation matrix $C_n = E(\bar{n}\bar{n}^T)$. C_n is an $N \times N$ full-rank symmetric matrix. There are N independent eigenvectors x_i corresponding to the N eigenvalues λ_i $(i = 1, 2, \ldots, N)$,

$$C_n \bar{x}_i = \lambda_i \bar{x}_i,$$

$$\bar{x}_i \bar{x}_j = \begin{cases} 1 & i = j \\ 0 & i \neq j \end{cases} \quad (i, j = 1, 2, \ldots N). \tag{A1}$$

Equation (A1) can be expressed by the matrix

$$C_n X = X\Lambda,$$

where

$$X = [x_1 \quad x_2 \cdots x_N],$$

$$\Lambda = \begin{bmatrix} \lambda_1 & 0 & \cdots & 0 \\ 0 & \lambda_2 & & 0 \\ \vdots & & \ddots & \\ 0 & 0 & & \lambda_N \end{bmatrix}. \tag{A2}$$

Matrix Λ represents the canonical form of C_n, a diagonal matrix with C_n's eigenvalues along the main diagonal. Matrix X denotes the modal matrix whose columns are the eigenvectors of C_n. Note that the operation on both XX^T and X^TX yields an identity matrix. Therefore, Eq. (A1) can be written as

$$C_n = X\Lambda X^T = X\Delta\Delta X^T = (X\Delta)(X\Delta)^T = BB^T, \tag{A3}$$

where

$$\Delta = \begin{bmatrix} \sqrt{\lambda_1} & 0 & \cdots & 0 \\ 0 & \sqrt{\lambda_2} & & 0 \\ \vdots & & \ddots & \\ 0 & 0 & & \sqrt{\lambda_N} \end{bmatrix},$$

$$B = X\Delta. \tag{A4}$$

Now the noise $\bar{n}$ vector can be expressed as a linear combination of N independent identically Gaussian distributed $\bar{n}_{gd}$ with zero mean and unit variance,

$$\bar{n} = B\bar{n}_{gd}. \tag{A5}$$

The cross-correlation matrix C_n of the noise is calculated by

$$C_n = E(\bar{n}\bar{n}^T) = E((B\bar{n}_{gd})(B\bar{n}_{gd})^T) = BE(\bar{n}_{gd}\bar{n}_{gd}^T)B^T = BB^T. \tag{A6}$$

APPENDIX B: DEFINITIONS

1. Signal-to-noise ratio

The signal-to-noise ratio (SNR_e) in elastography is a quantity used to describe the noise properties of the strain image. The SNR_e is defined as[24,25]

$$SNR_e = \frac{m_s}{\sigma_s}, \tag{B1}$$

where m_s and σ_s denote the mean and the standard deviation of estimated strain, respectively.

2. Contrast-to-noise ratio

The contrast to-noise ratio (CNR_e) is a quantity that determines the detectability of lesions.[26] The CNR_e for elastography is defined as follows:[26]

$$CNR_e = \frac{2(e_B - e_I)^2}{\sigma_{eB}^2 + \sigma_{eI}^2}, \tag{B2}$$

where e_B and e_I represent mean strain in the background and inclusion, while σ_{eB} and σ_{el} represent standard deviation of background and inclusion, respectively.

[a]Author to whom correspondence should be addressed. Electronic mail: tvarghese@wisc.edu; Telephone: (608)-265-8797; Fax: (608)-262-2413.

[1]J. Ophir, I. Cespedes, H. Ponnekanti, Y. Yazdi, and X. Li, "Elastography: A quantitative method for imaging the elasticity of biological tissues," Ultrason. Imaging **13**, 111–134 (1991).
[2]M. O'Donnell, A. R. Skovoroda, B. M. Shapo, and S. Y. Emelianov, "Internal displacement and strain imaging using ultrasonic speckle tracking," IEEE Trans. Ultrason. Ferroelectr. Freq. Control **41**, 314–325 (1994).
[3]T. Varghese, J. Ophir, E. Konofagou, F. Kallel, and R. Righetti, "Tradeoffs in elastographic imaging," Ultrason. Imaging **23**, 216–248 (2001).
[4]J. C. Bamber and N. L. Bush, "Freehand elasticity imaging using speckle decorrelation rate," Acoust. Imaging **22**, 285–292 (1996).
[5]K. J. Parker, S. R. Huang, R. A. Musulin, and R. M. Lerner, "Tissue response to mechanical vibrations for 'sonoelasticity imaging'," Ultrasound Med. Biol. **16**, 241–246 (1990).
[6]T. J. Hall, Y. Zhu, and C. S. Spalding, "In vivo real-time freehand palpation imaging," Ultrasound Med. Biol. **29**, 427–435 (2003).
[7]T. A. Krouskop, D. R. Dougherty, and F. S. Vinson, "A pulsed Doppler ultrasonic system for making noninvasive measurements of the mechanical properties of soft tissue," J. Rehabil. Res. Dev. **24**, 1–8 (1987).
[8]M. F. Insana, L. T. Cook, M. Bilgen, P. Chaturvedi, and Y. Zhu, "Maximum-likelihood approach to strain imaging using ultrasound," J. Acoust. Soc. Am. **107**, 1421–1434 (2000).
[9]B. S. Garra, E. I. Cespedes, J. Ophir, S. R. Spratt, R. A. Zuurbier, C. M. Magnant, and M. F. Pennanen, "Elastography of breast lesions: Initial clinical results," Radiology **202**, 79–86 (1997).
[10]U. Techavipoo, Q. Chen, T. Varghese, J. A. Zagzebski, and E. L. Madsen, "Noise reduction using spatial-angular compounding for elastography," IEEE Trans. Ultrason. Ferroelectr. Freq. Control **51**, 510–520 (2004).
[11]U. Techavipoo, Q. Chen, T. Varghese, and J. A. Zagzebski, "Estimation of displacement vectors and strain tensors in elastography using angular insonifications," IEEE Trans. Med. Imaging **23**, 1479–1489 (2004).
[12]M. Rao and T. Varghese, "Spatial angular compounding for elastography without the incompressibility assumption," Ultrason. Imaging **27**, 256–270 (2005).
[13]E. E. Konofagou, T. Harrigan, and J. Ophir, "Shear strain estimation and lesion mobility assessment in elastography," Ultrasonics **38**, 400–404 (2000).
[14]M. Rao, Q. Chen, H. Shi, T. Varghese, E. L. Madsen, J. A. Zagzebski, and T. A. Wilson, "Normal and shear strain estimation using beam steering on linear-array transducers," Ultrasound Med. Biol. **33**, 57–66 (2007).
[15]A. Thitaikumar, T. A. Krouskop, B. S. Garra, and J. Ophir, "Visualization of bonding at an inclusion boundary using axial-shear strain elastography: A feasibility study," Phys. Med. Biol. **52**, 2615–2633 (2007).
[16]F. Kallel, T. Varghese, J. Ophir, and M. Bilgen, "The nonstationary strain filter in elastography. II. Lateral and elevational decorrelation," Ultrasound Med. Biol. **23**, 1357–1369 (1997).
[17]S. I. Olsen, "Estimation of noise in images-An evaluation," CVGIP: Graph. Models Image Process. **55**, 319–323 (1993).
[18]M. K. Ozkan, M. I. Sezan, and A. M. Tekalp, "Adaptive motion-compensated filtering of noisy image sequences," IEEE Trans. Circ. Syst. Video Tech. **3**, 277–290 (1993).
[19]R. C. Gonzalez and R. E. Woods, *Digital Image Processing* (Prentice Hall, Englewood Cliffs, 2002).
[20]Y. Li and J. A. Zagzebski, "A frequency domain model for generating *B*-mode images with array transducers," IEEE Trans. Ultrason. Ferroelectr. Freq. Control **46**, 690–699 (1999).
[21]E. L. Madsen, G. R. Frank, T. A. Krouskop, T. Varghese, F. Kallel, and J. Ophir, "Tissue-mimicking oil-in-gelatin dispersions for use in heterogeneous elastography phantoms," Ultrason. Imaging **25**, 17–38 (2003).
[22]P. E. Barbone and A. A. Oberai, "Elastic modulus imaging: Some exact solutions of the compressible elastography inverse problem," Phys. Med. Biol. **52**, 1577–1593 (2007).
[23]J. Jiang, T. J. Hall, and A. M. Sommer, "A novel performance descriptor for ultrasonic strain imaging: A preliminary study," IEEE Trans. Ultrason. Ferroelectr. Freq. Control **53**, 1088–1102 (2006).
[24]T. Varghese and J. Ophir, "A theoretical framework for performance characterization of elastography: The strain filter," IEEE Trans. Ultrason. Ferroelectr. Freq. Control **44**, 164–172 (1997).
[25]I. Cespedes and J. Ophir, "Reduction of image noise in elastography," Ultrason. Imaging **15**, 89–102 (1993).
[26]T. Varghese and J. Ophir, "An analysis of elastographic contrast-to-noise ratio," Ultrasound Med. Biol. **24**, 915–924 (1998).